Labeling of Cancer Cells with Magnetic Nanoparticles for Magnetic Resonance Imaging

Christian Weis,[1]* Fabian Blank,[2] Adrian West,[3] Gregory Black,[4] Robert C. Woodward,[4] Matthew R.J. Carroll,[4] Astrid Mainka,[1] René Kartmann,[1] Andreas Brandl,[5] Heiko Bruns,[6] Elizabeth Hallam,[7,8] Jeremy Shaw,[9] John Murphy,[9] Wey Yang Teoh,[10] Katerina E. Aifantis,[11] Rose Amal,[12] Mike House,[4] Tim St. Pierre,[4] and Ben Fabry[1]

Purpose: The process of invasion and metastasis formation of tumor cells can be studied by following the migration of labeled cells over prolonged time periods. This report investigates the applicability of iron oxide nanoparticles as a magnetic resonance imaging (MRI) contrast agent for cell labeling.
Methods: γFe_2O_3 nanoparticles prepared with direct flame spray pyrolysis are biofunctionalized with poly-L-lysine (PLL). The nanoparticles within the cells were observed with transmission electron microscopy, bright-field microscopy, and magnetorelaxometry. MRI of labeled cells suspended in agarose was used to estimate the detection limit.
Results: PLL-coated particles are readily taken up, stored in intracellular clusters, and gradually degraded by the cells. During cell division, the nanoparticle clusters are divided and split between daughter cells. The MRI detection limit was found to be 25 cells/mm^3 for R2*, and 70 cells/mm^3 for R2. The iron specificity, however, was higher for R2 images. Due to the degradation of intracellular γFe_2O_3 to paramagnetic iron ions within 13 days, the R1, R2, and R2* contrast gradually decreased over this time period to approximately 50% of its initial value.
Conclusions: These results suggest that PLL-coated γFe_2O_3 nanoparticles can be used as an MRI contrast agent for long-term studies of cell migration. **Magn Reson Med 000:000–000, 2013. © 2013 Wiley Periodicals, Inc.**

Key words: molecular imaging; nanoparticles; relaxometry; cancer metastasis; magnetic resonance imaging; iron oxide

[1]Department of Physics, University of Erlangen-Nuremberg, Germany.

[2]Respiratory Medicine, Berne University Hospital, Berne, Switzerland.

[3]School of Anatomy, Physiology and Human Biology, University of Western Australia, Australia.

[4]School of Physics, University of Western Australia, Australia.

[5]Department of Plastic and Hand Surgery, Hospital of Erlangen, University of Erlangen-Nuremberg, Germany.

[6]Department of Internal Medicine 5 – Haematology/Oncology, University of Erlangen-Nuremberg, Germany.

[7]Australian National University, Canberra.

[8]Current address: ACT Government Health Directorate, Canberra Hospital and Health Services, Canberra, Australia.

[9]Centre for Microscopy, Characterisation and Analysis, University of Western Australia, Australia.

[10]School of Energy and Environment City, University of Hong Kong, Kowloon, Hong Kong SAR.

[11]Laboratory of Mechanics and Materials, Aristotle University of Thessaloniki, Greece.

[12]School of Chemical Sciences and Engineering, University of New South Wales, Australia.

*Correspondence to: Christian Weis, Biophysics, Department of Physics, University of Erlangen-Nuremberg, Henkestrasse 91, 91052 Erlangen, Germany. E-mail: cweis@biomed.uni-erlangen.de

The malignancy of cancer is associated with the ability of tumor cells to metastasize in distant organs. The migration of tumor cells through connective tissue and in and out of the blood or lymph system is a prerequisite for metastasis formation. The common approach to follow the formation and progression of metastases in animal models is to sacrifice the animal for data collection. Therefore, the information that can be obtained from an individual animal is limited to a single time point. Non-invasive imaging techniques such as bioluminescence imaging, computed tomography, or magnetic resonance imaging (MRI) have the potential to circumvent this problem. They can, however, suffer from insufficient resolution and other practical constraints, making them unsuitable to follow the migration of a small number of tumor cells. Secondary tumors can only be monitored and characterized with these techniques after they have grown to an appreciable size.

To cope with these problems, it has been suggested to increase the sensitivity and specificity of MRI for tumor cell detection by labeling the cells with iron oxide-based contrast agents (1). Tumor cell migration, regional tumor growth, and micrometastatic progression could be investigated by labeling in vitro cultures of metastatic tumor cells with iron oxide particles, injecting these cells into an animal, and tracking them over time with MRI. This strategy has been applied to detect iron oxide-labeled metastatic melanoma cells within the mouse lymph nodes (2). In that study, melanoma cells were incubated with magnetite-loaded 0.9 μm polystyrene beads prior to injecting the cells into the lymph nodes of mice. As few as 100 cells could be detected by using a proprietary balanced steady-state free precession imaging sequence (GE's FIESTA sequence). As the tumors grew over time at the site of injection, the signal gradually faded. It was

unclear, however, whether the signal loss was attributable to a dilution of the magnetic particles due to tumor cell growth and division, or whether the cells progressively metabolized or released iron over time. If the cells were not injected into the animal but were further allowed to grow in the culture dish, there was a complete loss of detectable iron within 5 days after particle incubation, corresponding to six cell division cycles (2). A similarly rapid loss of iron oxide has also been observed in HeLa cancer cells under in vitro culture conditions (3).

This study explores the application of iron oxide nanoparticles for monitoring tumor growth and metastasis progression over extended periods of time. This includes the uptake of iron oxide particles by cancer cells, the influence that the particles may have on the cells' metastatic behavior, the long-term stability of the particles in the cells, their magnetic behavior, and their R1, R2, and R2* proton relaxivities during MRI.

METHODS

Cells

Cell experiments were conducted on a transformed bronchial epithelial cell line (16HBE14o), on freshly isolated pig tracheal smooth muscle cells, and on a human breast carcinoma cell line (MDA-MB-231). 16HBE14o and MDA-MB-231 cells were grown in Dulbecco's modified Eagle's medium (DMEM) with 10% fetal bovine serum (FBS), 25 mM 4-(2-hydroxyethyl)-1-piperazineethanesulfonic acid (HEPES), 1% L-glutamine, and 1% penicillin/streptomycin. Cells were detached with trypsin/ethylenediaminetetraacetic acid (EDTA), reseeded in 35 mm culture dishes at 200,000 per well and grown for 2 days until confluent.

Porcine airway smooth muscle cultures were derived from freshly removed trachealis muscle using previously described methods (4) and grown in DMEM with 10% FBS (FBS), 100 U/mL penicillin, 100 μg/mL streptomycin, 50 μg/mL gentamycin, 0.1 mM nonessential amino acids, and 2 mM glutamine for 7 days. Cells were detached with trypsin/EDTA, reseeded in 35 mm culture dishes at 100,000 cells per well, and grown for 3 days until confluent. The cells were serum deprived by replacing FBS with 1% insulin-transferrin-selenium supplement immediately prior to being loaded with magnetic particles for 24 hr.

Magnetic Particles

Iron oxide nanoparticles have previously been shown to be nontoxic, bioinert up to concentrations of 100 μg/mL (1–3,5,6), and to act as a strong enhancer of proton spin dephasing (1,7). Hence, they are extensively used as a contrast agent in MRI. A wide range of commercial and noncommercial iron oxide particles and a similarly wide range of different particle surface functionalizations to enable cell entry have been used in these studies. A clear preference or advantage of any specific particle or surface functionalization is not obvious from published data. For reasons of availability and, as described below, quick uptake by the cells as well as advantageous magnetic properties, we used γFe_2O_3 iron oxide (maghemite) nanoparticles (8) produced by flame spray pyrolysis (FSP). Particles were either purchased from Sigma or were fabricated using a custom-made FSP reactor at the University of New South Wales (UNSW) (9).

Cell Labeling

To facilitate particle uptake by the cell, the particles were coated with poly-L-lysine (PLL) by incubating them overnight in a 0.01% (w/v) PLL solution (10). Unless noted otherwise, 50 μg of nanoparticles were added to confluent cells grown in a 35 mm plastic cell culture dish, and incubated for 24 hr. This corresponds to approximately 1 μg of particles per 10,000 cells.

Transmission Electron Microscopy

Cells to be examined by transmission electron microscopy (TEM) were cultured on 10 mm plastic coverslips (Therminox) and incubated with either Sigma or UNSW iron oxide particles for 24 hr. Samples were fixed with 2% glutaraldehyde in phosphate buffered saline (PBS) for 24 hr and postfixed in OsO_4 for 30 min, then dehydrated in a graded series of ethanol prior to embedding in Spurrs hard resin. Sections for TEM were cut to a thickness of ∼80 nm, mounted on copper grids and imaged at 120 kV (JEOL, JEM 2100) using an 11Mpix CCD camera (Gatan, Orius1000).

Bright-Field Microscopy

If not specified otherwise, cells were cultured in 35 mm plastic cell culture dishes, labeled with iron oxide particles as described above, detached with trypsin/EDTA, and reseeded at a density of 50,000 cells per 35 mm well, or 200,000 cells per 75 cm² cell culture flask. Cells were then monitored continuously or intermittently over prolonged time periods for up to 9 days. Iron oxide particle content per cell before and after cell division was estimated from bright-field images after image binarization and area estimation using custom image analysis programs written in MATLAB.

Long-Term Stability Assay

To characterize the long-term stability of the particles in the cells, freshly isolated pig tracheal smooth muscle cells were loaded with either Sigma or UNSW particles for 24 hr (100 μg of particles per 35 mm dish). Cells were serum starved for different time periods of up to 3 weeks, after which their iron content was measured with inductively coupled plasma mass spectrometry. Airway smooth muscle cells tolerate serum starvation but do not divide and proliferate under such conditions.

Cell-Division Assay

To investigate the partitioning of nanoparticles during cell divisions, we performed two sets of experiments. In the first set, epithelial cells were incubated with Sigma particles for 24 hr, and 200,000 cells were replated in a 75 cm² cell culture flask. Over the following days, bright-field microscopy images were recorded at random positions. The area densities of the particle clusters were quantified by image segmentation with a threshold set to 50% of the maximum brightness. The number of black pixels per image was taken as the area density of the

particle clusters and was interpreted as an estimate of the particle concentration within the cells. In the second set of experiments, MDA-MB-231 cells were incubated with iron oxide particles for 24 hr (50 μg of particles for 500,000 cells), and 50,000 cells were replated in 35 mm dishes. Over the following 3 days, bright-field microscopy images were taken at 5 min intervals at multiple positions. We analyzed in total 105 cell divisions.

Proliferation Assay

To measure the proliferation rates, MDA-MB-231 cells were incubated with Sigma iron oxide nanoparticles for 24 hr as described above, and 80,000 cells were replated in 35 mm dishes. Cells were harvested 24, 48, or 72 hr after labeling and counted with a hemocytometer (Neubauer chamber). The time between cell divisions T was calculated from the cell number N_t at different time points t according to the relationship $N_t = N_0 2^{t/T}$, with N_0 being the initial number of cells ($N_0 = 80,000$).

Viability Assay

Cell viability of MDA-MB-231 cells incubated with Sigma iron oxide nanoparticles for 24 or 72 hr was analyzed with fluorescence-activated cell sorting (FACS) (FACScalibur, BD Biosciences, San Jose, CA) using propidium iodide (PI) for staining dead cells. Cells were harvested with trypsin/EDTA and resuspended in 400 μl FACS buffer (phosphate-buffered saline with 2% FBS). Prior to FACS measurements, 1 μl of PI was added to the cells. A bimodal log-normal distribution was fitted to the histogram data from 10,000 cells. All cells contributing to the higher-intensity mode were counted as dead cells.

Reactive Oxygen Species Assay

MDA-MB-231 cells incubated with Sigma iron oxide nanoparticles for 48 hr were harvested with trypsin/EDTA, resuspended in 400 μl FACS buffer, and stained with 50 μM 2′,7′-dichlorfluorescein-diacetate for 30 min at 37°C. The dye is converted to the fluorescent 2′,7′-dichlorfluorescein (DCF) in the presence of reactive oxygen species (ROS) (11). Mitochondrial ROS production was detected using MitoSOX Red fluorescent staining (2 μM for 30 min at 37°C) (Invitrogen, Carlsbad, CA). After 30 min of staining, cells were rinsed two times with 4°C cold FACS buffer to wash off unbound dye and kept on ice. Fluorescence intensities of 10,000 cells from each sample were measured with a FACS-Canto II (BD Biosciences, San Jose, CA). Unstained unlabeled cells as well as unstained but iron-oxide labeled cells were also measured for background correction. For a positive control, cells were incubated with H_2O_2 (10 μM for 2 hr at 37°C) before harvesting and ROS staining.

Contractility Assay

To quantify the contractile forces during invasion in a 3D collagen gel, the elastic strain energy stored in the matrix due to traction-induced deformations was measured (12). To avoid bias toward cells that are able to spontaneously invade the matrix, cells were mixed in collagen solution containing fluorescent beads prior to polymerization. The matrix deformations around single cells were quantified by tracking the 3D position of the surrounding fluorescent beads. From the bead displacements and the known matrix elasticity, the local strain energy in the matrix surrounding the cell was then computed. MDA-MB-231 breast carcinoma cells were labeled with 50 μg iron oxide per 500,000 cells (particle uptake was 90 pg/cell on average as measured by ferrozine-based colorimetric spectroscopy) and mixed in a collagen solution containing fluorescent latex beads prior to collagen polymerization. The local strain energy was calculated for 10 control cells and 10 cells labeled with iron oxide.

Collagen Invasion Assay

To characterize and compare the invasion and migration behavior of the cells, a 3D collagen invasion assay was performed (13). Cells were seeded on top of a collagen gel and cultured for 72 hr at 37°C, 5% CO_2, and 95% humidity in DMEM. During this time, cells spontaneously invaded into the depths of the collagen gel. MDA-MB-231 breast carcinoma cells were incubated with different nanoparticle concentrations (0, 0.62, and 50 μg iron oxide per 500,000 cells) for 24 hr, and reseeded in 35 mm petri dishes on top of thick (0.5 mm) reconstituted collagen matrices. MDA-MB-231 are able to spontaneously invade into such matrices (13). After 3 days of invasion, the cells were fixed with 2.5% glutaraldehyde, and the cell nuclei were stained with Hoechst 33342. A motorized microscope was used for imaging z-sections with a separation of 2 μm through the entire collagen gel. The percentage of invasive cells and the cell density as a function of their invasion depths were determined in 25 randomly chosen field of views.

Relaxometry

The spin–spin relaxation rate (R2) of protons surrounding the magnetic particles was measured in a 1.4 T relaxometer (Bruker Minispec). Nanoparticles or cells were diluted in a 2% agarose solution, and measurements were performed at 37°C with a multi-spin-echo pulse sequence (interecho spacing of 0.4 ms). Agarose was used because it exhibits a relaxation behavior similar to human tissue.

Saturation Magnetization Assay

Magnetization curves of γFe_2O_3 nanoparticles (Sigma) were measured at different time points after internalization into cells (MDA-MB-231) using a commercial 5 Tesla Superconducting Quantum Interference Device (SQUID, Quantum Design, MPMS-XL) in DC mode. The saturation magnetization for each sample was computed from the magnetization curves using a Langevin function (14) and was corrected by subtracting the field-dependent magnetization of the sample holder and the cells without iron oxide particle labeling. The amount of iron in each sample was quantified by ferrozine-based colorimetric spectroscopy (15) in order to normalize the saturation magnetization to the iron mass.

Magnetic Resonance Imaging

To estimate the detection limit of magnetically labeled cells in an MRI scanner, the cells were suspended in a
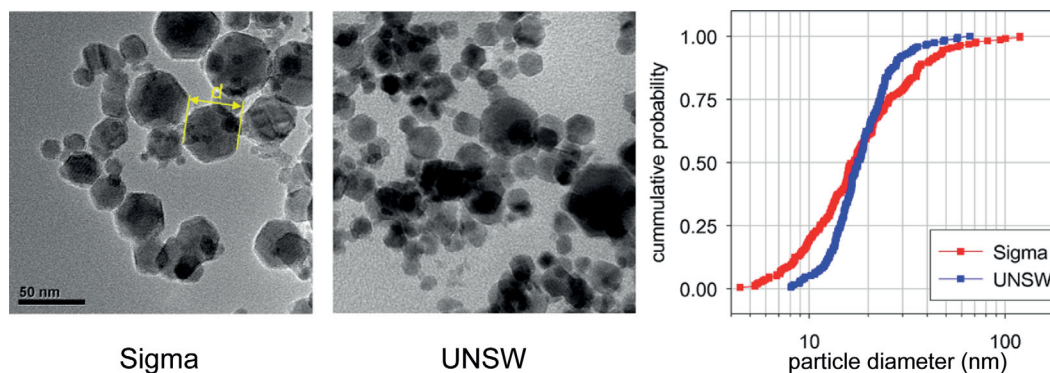
FIG. 1. TEM images of Sigma (left) and UNSW (middle) particles. Right: distribution of particles diameter as defined in the left image. [Color figure can be viewed in the online issue, which is available at wileyonlinelibrary.com.]

2% agarose solution. A 1:3 dilution series was filled in 2 ml Eppendorff test tubes and placed in a 1.5 T MRI medical scanner (Siemens Medical Solutions, Erlangen, Germany). The R2 and R2* relaxation rates were computed from a mono-exponential fit of the signal decay at seven different spin echo or gradient echo delay times, ranging from 4 to 100 ms. The in-plane scan resolution was 1x1 mm, and the slice thickness was set to 5 mm. The detection limit was defined as the particle concentration at which the relaxivity signal from the voxels inside the test tubes increased above the agar background value with a statistical significance of $P < 0.001$.

To test whether the MRI signals deteriorates when the nanoparticles are exposed to the intracellular environment over extended time periods, R1, R2, and R2* relaxation rates were measured after different incubation times with a 4.7 T Bruker BioSpin MRI system. The spin lattice relaxation (R1 = 1/T1) was obtained with a sequence of spin echo protocols with logarithmically spaced inversion recovery times between 60 and 3500 ms. The (corrected) spin–spin relaxation (R2 = 1/T2) was measured with a RAREVTR sequence (TE: 11:22:99 ms (first echo:echo spacing:last echo), TR: 1500 ms). The spin–spin relaxation (R2* = 1/T2*) was quantified using a multigradient echo (MGE) sequence (TE: 4.5:7:81.5 ms, TR: 1500 ms). The spatial resolution was 0.39 mm in frequency direction and 0.21 mm in phase direction, the slice thickness was 6 mm. Three samples were imaged: a 2% agarose sample without cells, a sample containing 2% agarose mixed with freshly Sigma Fe_2O_3-labeled cells (0.5-day incubation time), and a sample containing 2% agarose mixed with long-term labeled cells (14 days incubation time). To compare R1, R2, and R2* for both incubation times (0.5 and 14 days), the cell samples were loaded with the same amount of iron ($2.5 \cdot \times 10^6$ cells, labeled with 1 μg Fe_2O_3 per 10,000 cells, mixed with 1 ml 2% agarose gel).

RESULTS

Particle Size

TEM imaging showed that both Sigma and UNSW particles synthesized by FSP form hexagonal crystals. The median diameter of Sigma particles was 17 nm, and the median diameter of UNSW particles was 17.7 nm. Sigma particles showed a wider distribution of particle sizes

(interquartile range of 14 nm) compared to UNSW particles (interquartile range of 8.6 nm) (Fig. 1).

Particle Clustering

Both Sigma and UNSW particles formed aggregates, or clusters, of varying sizes. Volume-weighted dynamic light scattering (DLS) revealed a bimodal, log-normal distribution of cluster sizes. In the case of Sigma particles, 706 nm clusters formed the majority (80 vol %) of the sample, whereas smaller 63 nm clusters contributed only 20 vol %. In the case of UNSW particles, both larger (159 nm) and smaller (36 nm) clusters contributed approximately equally to the volume of the sample. It is not clear from DLS analysis, however, whether the smaller size fraction consisted of small, clustered nanoparticles or larger sized, single nanoparticle crystals.

Cell Uptake

Both Sigma and UNSW particles or particle clusters bound avidly to the cell surface and were readily taken up by the cells. Within the cells, nanoparticle clusters were often compartmentalized and formed super-clusters with diameters spanning up to 10 μm (Fig. 2a,b).

In the case of UNSW particles, a small fraction of clusters was found extracellularly but associated with the cell surface (Fig. 2c). The iron oxide content of the lavage fluid, or supernatant, aspirated from the cell wells after a particle incubation time of 24 hr was below the detection limit of inductively coupled mass spectrometry, suggesting that close to 100% of the particles were either bound or taken up by the cells.

Long-Term Stability

The amount of intracellular iron in nondividing, serum-starved trachealis smooth muscle cells was measured with inductively coupled plasma mass spectrometry and remained constant over the time course of 18 days for both Sigma and UNSW particles (Supporting Information Fig. 1A).

Cell Division

Over the time course of 9 days after reseeding particle-loaded transformed bronchial epithelial cells, the size of intracellular particle clusters decreased as the cells
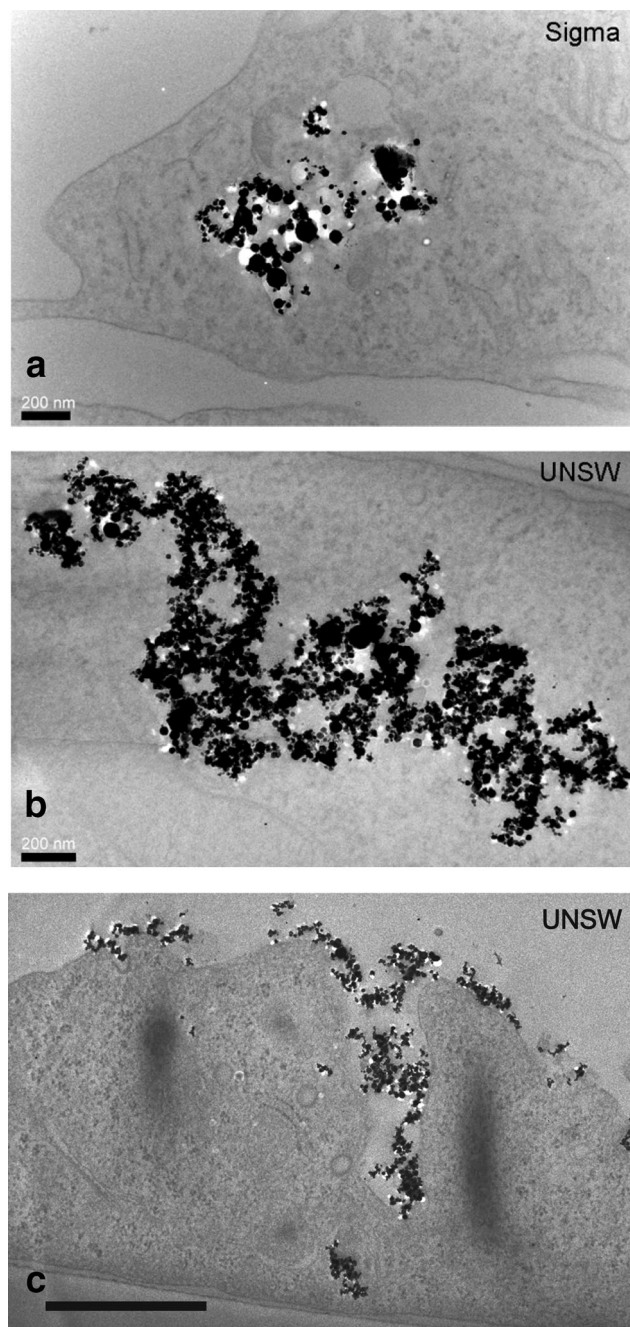
FIG. 2. TEM image of particles during and after the uptake by transformed bronchial epithelial cells. **a**: Sigma particles (Scale bar is 200 nm). **b**: UNSW particles (scale bar is 200 nm). **c**: Transformed bronchial epithelial cell in the process of UNSW nanoparticle uptake by membrane invagination (scale bar is 1 μm).

divided, suggesting that the particle clusters can be broken apart during cell division and can be distributed among the daughter cells. The area density of the particles also decreased, which was not caused by a loss of iron oxide content but was attributable to the fact that this method is biased toward larger clusters because of their better contrast. Very small clusters that emerge as the larger clusters are broken apart over time cannot be reliably detected by bright-field microscopy. Nonetheless, we did not see a complete loss of particles as reported

previously for rapidly dividing cells (2,3). The experiment was terminated when the cells grew over-confluent after 9 days in culture and started to round up and detach from the substrate (Supporting Information Fig. 1B,C).

To further explore how particle clusters are partitioned to the daughter cells during cell division, we continuously recorded bright-field images over a time course of 60 hr (Fig. 3, top). A total of 105 cell divisions were analyzed in detail. In 10% of all cell divisions, the magnetic material was approximately evenly divided among the daughter cells (Fig. 3, bottom). In 52% of cell divisions, however, at least 90% of the magnetic material of the mother cell was given to one daughter cell, with the other daughter cell receiving 10% or less.

Proliferation Rate and Cell Viability

Labeling with PLL-coated Sigma nanoparticles had no effect on proliferation rate and cell viability of MDA-MB-231 cancer cells. The time between cell division (T) for the labeled and unlabeled cells was nearly identical (Fig. 4a). Twenty-four hours after incubation with Fe_2O_3, the fraction of dead cells was $6.41 \pm 0.87\%$ (mean $\pm$ SE), compared with $5.14 \pm 1.35\%$ for the unlabeled cells (Fig. 4b). These differences were small and not
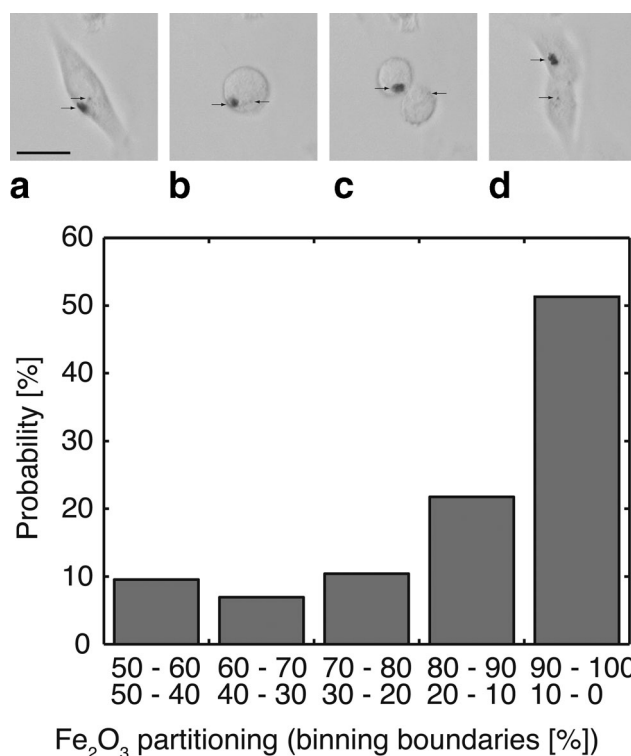

FIG. 3. Top: Bright-field images of an MDA-MB-231 cell incubated with iron oxide particles (scale bar is 25 μm). This image sequence shows the partitioning of two nanoparticle clusters (indicated by arrows) during cell division (**a**: Before cell division, **b**: Anaphase, **c**: Cytokinesis, **d**: After cell division). The smaller cluster was not in the focal plane in images B and C. Bottom: Partitioning of iron oxide particles during cell division. A partitioning of 50:50 ... 60:40 was observed in 9% of all cell divisions, whereas a partitioning of 90:10 ... 100:0 was observed in 52% of all cell divisions. The mean partitioning ratio was 85:15.
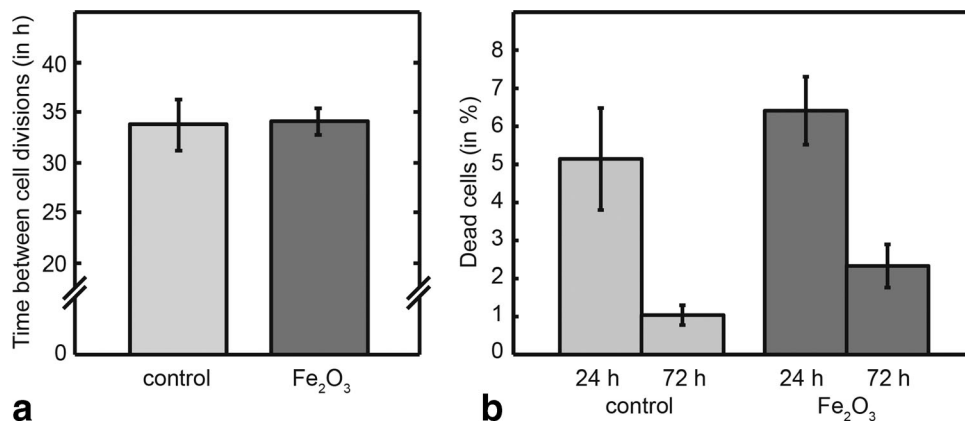
FIG. 4. **a**: Time between cell divisions (T) of unlabeled and the labeled cells is similar. Cell number was measured 0, 24, 48, and 72 hr after seeding. $T_{unlabeled\ cells} = 33.87 \pm 2.54$ hr (mean $\pm$ SE, $n = 6$ wells), $T_{labeled\ cells} = 34.16 \pm 1.24$ hr, $n = 6$ wells. **b**: Cell viability was analyzed with flow cytometry of propidium iodide stained cells to count the number of dead cells after 24 and 72 hr. There was no significant difference between the labeled and unlabeled cells. Bars represent mean $\pm$ standard error from six wells.

statistically significant. Similarly, no statistically significant differences in cell viability were found after 72 hr of incubation with Fe_2O_3 nanoparticles (fraction of dead unlabeled cells: $1.04 \pm 0.24\%$, fraction of dead labeled cells: $2.33 \pm 0.51\%$).

ROS Assay

In addition to functional toxicity studies (proliferation rate, viability), we evaluated the intracellular production of ROS (Fig. 5a,c) as well as the mitochondrial ROS production (Fig. 5b,d) that may have resulted from the internalization and presence of iron oxide nanoparticles. FACS measurements of intracellular ROS concentration measured from DCF fluorescence in unlabeled and labeled cells 48 hr after incubation with Sigma particles showed no significant difference (Fig. 5a). Mitochondrial ROS production, measured with MitoSOX dye, was increased in the labeled cells (Fig. 5b), but this increase was small compared to an H_2O_2 positive control and was not statistically significant compared to unlabeled cells.

Contractile Forces

The ability of cells to migrate through a dense, porous 3D connective tissue matrix requires the generation of traction forces (12). Traction forces in 3D were measured by integrating the elastic strain energy in a collagen gel surrounding a single cancer cell. Our data show that nanoparticles have no inhibiting effect on contractile forces in a 3D collagen matrix (Fig. 6a,b).

Influence of Nanoparticles on Cell Invasion

We tested whether the nanoparticles interfered with the ability of the cells to invade a 3D extracellular matrix. The invasion profiles, expressed as the cumulative probability to find a cell at a certain depth or deeper, did not differ between nanoparticle-loaded cells and control cells (Fig. 6c). The differences at larger invasion depths (>175 µm) were caused by less than 2% of the cells and did not show a clear dependence on the amount of

nanoparticle loading, suggesting that the iron oxide labeling does not influence cell migration behavior.

Magnetic Properties

The R2 relaxivity of UNSW particles was 236 s^{-1} mM^{-1}, which is approximately 3 times greater than the R2 relaxivity induced by the same concentration of Sigma particles (79 s^{-1} mM^{-1}). This faster relaxation behavior of UNSW particles, which would lead to stronger MRI contrast, was much less pronounced in cells, however. The R2 relaxivity of cells loaded with UNSW particles was reduced to 103 s^{-1} mM^{-1}, while the R2 relaxivity from Sigma particles in cells was only marginally reduced to 64 s^{-1} mM^{-1} (Fig. 7a,b).

Magnetic properties of the iron oxide particles were measured at a temperature of 300 K in a SQUID magnetometer equipped with a 7 T coil. γFe_2O_3 iron oxide particles are superparamagnetic with a saturation magnetization of 66 emu/g (Sigma particles) or 63 emu/g (UNSW). Remanent magnetization was 16 emu/g in Sigma particles and 5 emu/g in UNSW particles.

To test if the magnetic properties remain stable in the intracellular environment, we measured Sigma particle-loaded cells at multiple time points after initial particle loading in a magnetometer. The saturation magnetization decreased by approximately 5 emu/g/day (Fig. 7c) and reached zero after 13 days. These findings indicate that the cell successively degrades the superparamagnetic iron oxide particles into free paramagnetic iron ions (14).

Magnetic Resonance Imaging

The detection limit of the R2* relaxation rate above the agarose background was 25 cells/mm^3, and the R2 detection limit was 70 cells/mm^3 (Fig. 8a,b). The iron specificity, however, was higher in the spin-echo R2 image, whereas the gradient-echo R2* image suffered from non-iron artifacts and signal distortions at the highest iron concentrations (Fig. 7a left).

In addition to the magnetometer measurements (Fig. 7c), MRI was performed to quantify long-term changes in
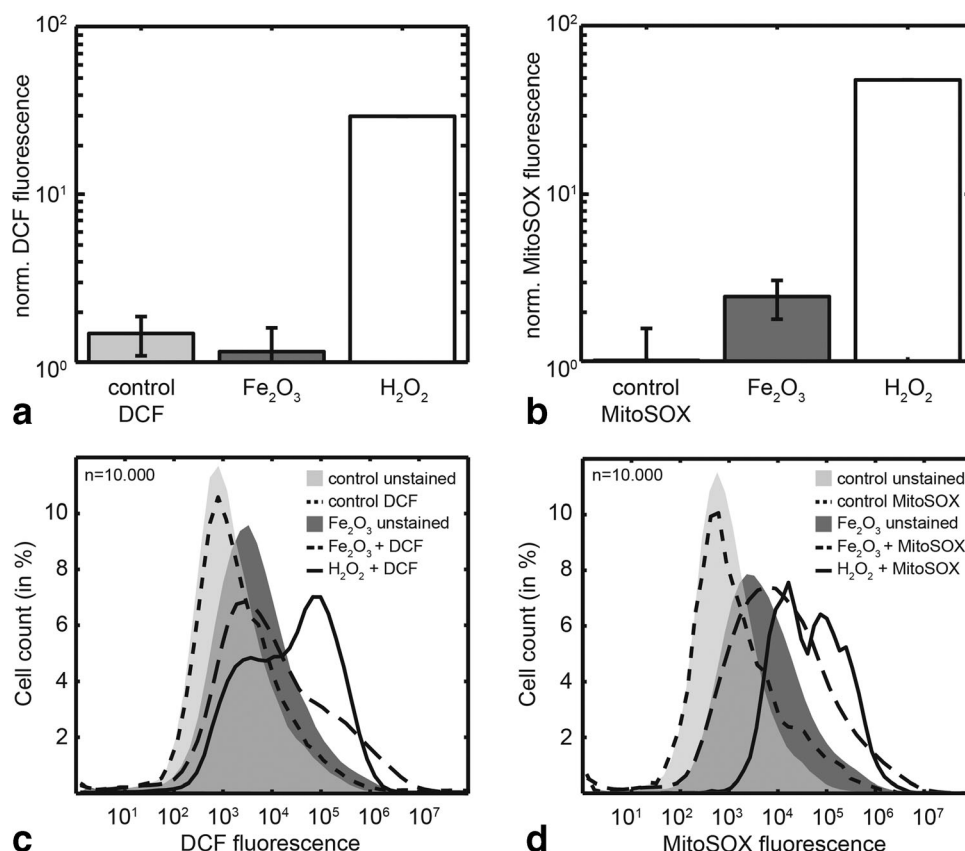
FIG. 5. Reactive oxygen species (ROS) production was quantified 48 hr after labeling with Sigma iron oxide nanoparticles by staining the cells for 30 min with 2′,7′-dichlorfluorescein-diacetate (total ROS production) and MitoSOX Red (mitochondrial ROS production). Fluorescence staining intensity as a measure of ROS production was quantified with flow cytometry on 10,000 cells per sample. The fluorescence intensities in **a** and **b** were background corrected by normalizing with the corresponding unstained cell sample. **a**: Unlabeled cells (control 2′,7′-dichlorfluorescein (DCF), $n = 2$ wells) and nanoparticle-labeled cells (Fe_2O_3, $n = 3$ wells) show no difference. For a positive control, cells were treated for 2 hr with 10 μM of H_2O_2, resulting in a 20-fold increase in ROS production. **b**: Mitochondrial ROS production was slightly (twofold) but not significantly increased in nanoparticle-labeled cells ($n = 3$ wells) compared to control ($n = 2$ wells). Treatment with 10 μM of H_2O_2 resulted in a 40-fold increase in ROS production. **c** and **d**: Histograms (50 logarithmically spaced bins) of fluorescence intensities for DCF (C) and MitoSOX Red (D) for all conditions. Histograms from the unstained cells were used for background correction. Note that iron oxide labeling results in a right shift of the histograms due to autofluorescence.

the magnetic properties after the nanoparticles were internalized by the cells. The enhancement of R1, R2, and R2* over the agarose background (contrast) decreased with time; after 14 days (at which time point the nanoparticles have been degraded to free paramagnetic iron ions), R1 contrast decreased to 21%, R2 contrast decreased to 45%, and R2* contrast decreased to 53% of the contrast produced by freshly labeled cells (Fig. 8c).

DISCUSSION

This study investigates the long-term behavior of γFe_2O_3 iron oxide nanoparticles in living cells, in particular, the intracellular uptake and distribution, the partitioning of particles during cell division, and the magnetic properties. The particles were produced by FSP and displayed a median diameter of 17 nm (Fig. 1). We compared a commercially available product (Sigma Aldrich) and custom-made particles (UNSW) that differed in their size distribution, with a broader distribution of the Sigma particles. In aqueous solution, both particle types form larger clusters that again differed, depending on particle source, with larger cluster of around 700 nm seen in the Sigma clusters, compared to cluster sizes on around 150 nm in the case of the custom-made particles. The magnetic properties were only marginally different between the two samples, with the UNSW sample having slightly lower magnetization due to a slightly lower degree of vacancy ordering (8). There was, however, a considerable difference in R1 and R2 relaxation rates, with lower values for the Sigma particles (Fig. 7a,b), which would result in less-favorable MRI contrast. However, once the particles were taken up by the cell, the differences in the relaxation rates were smaller.

These differences in the relaxation rates between particles and after particle internalization are explained by the static dephasing and echo-limiting regime theory (16,17). Accordingly, the differences in the R2 relaxation behavior between Sigma and UNSW particles, and between stock solutions and particles internalized by cells (Fig. 7a,b), are attributable to the particle aggregate size and the spatial homogeneity of the particle distribution (7). DLS measurements of the particles in suspension indicate that Sigma clusters are larger and make up
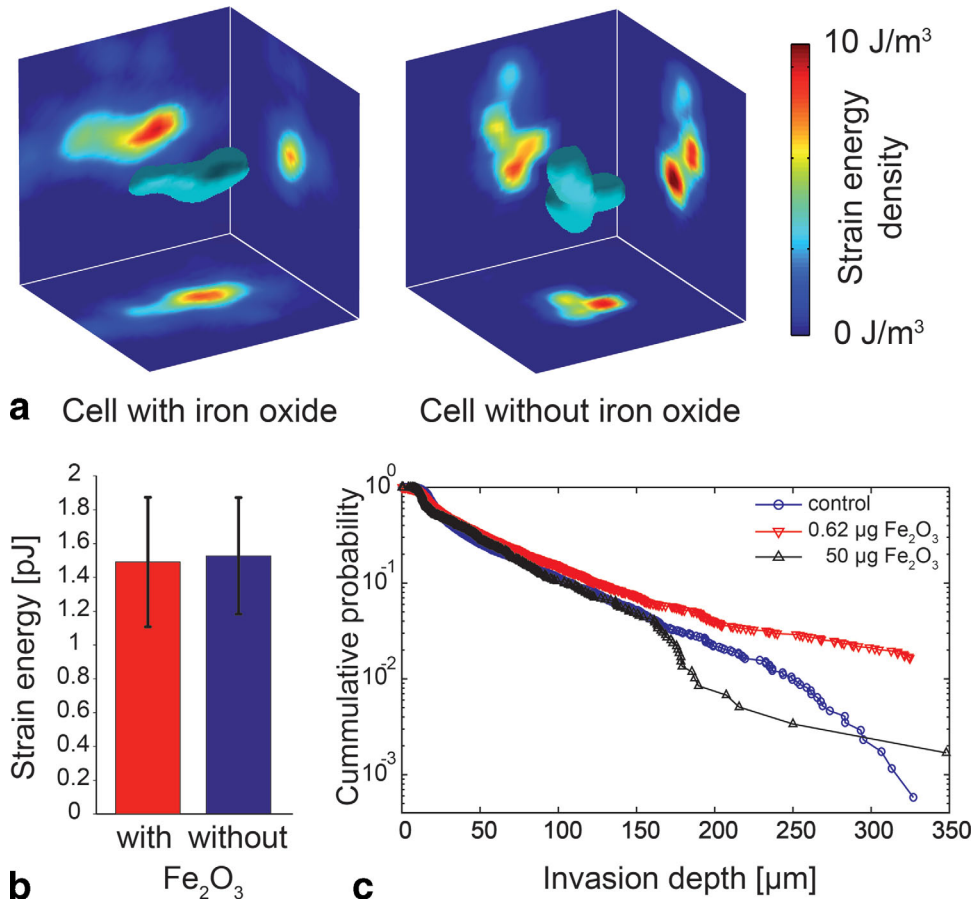
FIG. 6. Cell contractility and migration in a 3D collagen matrix. **a**: Strain energy density around a Sigma iron-oxide labeled (left) and unlabeled (right) MDA-MB-231 breast carcinoma cell in a 3D collagen gel. A strain energy density of 4 J/m^3 was chosen as the isosurface contour. **b**: Integration of the strain energy density around the cell gives the total strain energy. Cell loading with iron oxide nanoparticles caused no statistically significant change of strain energy. **c**: Invasion profiles of unlabeled and labeled cells. The probability to find a cell at or below a certain invasion depth did not differ between cells with or without nanoparticles. The differences at larger invasion depths were caused by less than 2% of the cells and did not show a clear dependence on the amount of nanoparticle loading. [Color figure can be viewed in the online issue, which is available at wileyonlinelibrary.com.]

a greater percentage of the total volume (80%), compared to UNSW particles (50%). Hence, the proportion of Sigma clusters in the echo-limited regime is likely to be much greater. This reduces the transverse relaxivity of the Sigma stock solution compared to the UNSW system. A theoretical and numerical validation can be found in Supporting Information. The large reduction in the transverse relaxivity of the UNSW particles, once they are internalized, suggests that the particles aggregate in the cells and become "echo-limited." The TEM images support this interpretation, showing large "super-clusters"

with sizes of up to 10 μm in diameter. As the size of UNSW clusters increases after internalization, the differences in the relaxivities between the Sigma and UNSW particles were less pronounced. We therefore focused in our long-term studies on the Sigma particles only, for reasons of their standardized properties, commercial availability, and low cost.

Sigma and UNSW particles are readily internalized by the cells, with a small portion that is bound to the cell surface (Fig. 2). An accumulation of free radicals and an increase in ROS production has been reported for cells in the presence
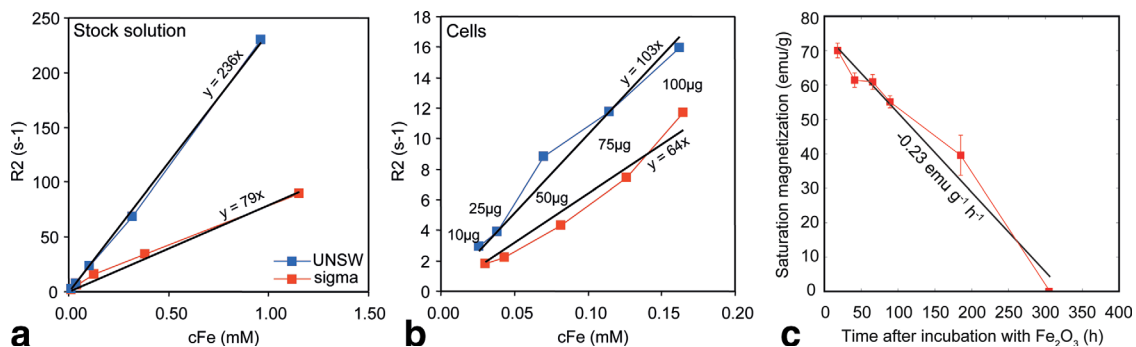

FIG. 7. **a,b**: Relaxation rate (R2) versus molar iron concentration for nanoparticles in stock solution (a) and in cells after 24 hr of incubation (b). Cells in a 35 mm culture dish were incubated with 10, 25, 50, and 100 μg of nanoparticles (see numbers in left diagram). Cell concentration during relaxation measurements was approximately 150,000 cells/ml. **c**: Saturation magnetization of intracellular γFe_2O_3 normalized to the amount of iron oxide and corrected by the diamagnetic magnetization of the sample holder and the cells versus time after incubation of the cancer cells with the nanoparticles. Error bars represent the uncertainty of intracellular γFe_2O_3 mass estimation by colorimetric spectroscopy. Saturation magnetization decreases over time at a rate of 0.23 emu g^{-1} h^{-1}.
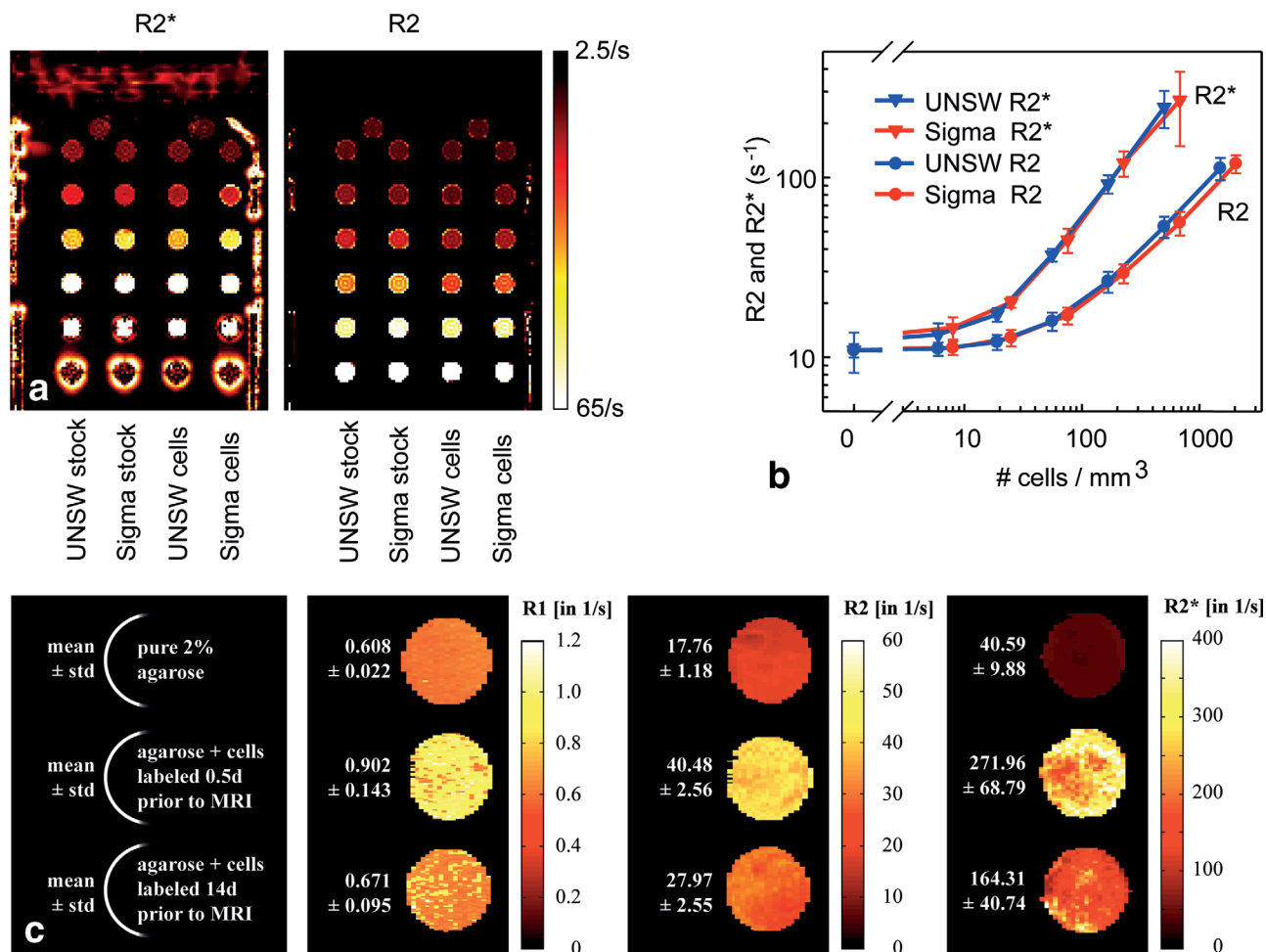
FIG. 8. **a**: MRI of dilution series of cells suspended in 2% agarose was used to estimate the detection limit. The R2* (left) and R2 (right) images demonstrate that the R2* signal gives a better detection limit, but the R2 signal has better iron specificity. The color map of the images scales linearly with the relaxation rate and was cropped at a maximum intensity corresponding to a relaxation rate of 65/s. **b**: The R2 and R2* relaxation rates were computed from the monoexponential signal decay sampled at 7 different echo time intervals. Mean and standard deviation of the relaxation rates within the area of each test tube are shown. **c**: Spin lattice (R1), (spin echo) spin–spin relaxation (R2), and (gradient echo) spin–spin (R2*) relaxation rates of intracellular nanoparticles for two different incubation times. The freshly labeled cells containing superparamagntic nanoparticles from Sigma have a higher influence on the relaxation rates than the cells labeled 14 days prior to MRI, compared to pure agarose.

of iron oxide nanoparticles (18). ROS are implicated in numerous toxic effects at the cellular level (18). Intracellular ROS production, measured with DCF, however, was not increased in the presence of intracellular Sigma iron oxide nanoparticles (Fig. 5a). Mitochondrial ROS production, measured with MitoSOX, was slightly but not significantly increased after 48 hr of incubation with Sigma particles (Fig. 5b). In agreement with these finding, the viability of cells labeled with iron oxide nanoparticles was not impaired (Fig. 4b) even after 72 hr of exposure.

During cell division, the intracellular super-clusters of nanoparticles are broken apart (Fig. 3, top b,c) and are distributed among the daughter cells (Fig. 3, bottom). On average, the partitioning is such that one daughter cell receives 85% of the magnetic material, and the other cell receives 15%. Knowledge of the partition ratio is important for interpreting the source of magnetic signal loss over time. A partitioning ratio of 50:50 would lead to an exponential decrease in the magnetic signal from each cell with a decay half-life of $-T^* \ln(2)/\ln(0.5)$, with T being the time between cell divisions, which was approximately 34 hr in the case of MDA-MB-231 cells (Fig. 4a). Therefore, cells that migrate away from their primary injection site could not be followed over prolonged time periods. In the case of a partitioning ratio of 85:15, the decay half-life is greatly prolonged to approximately $-T^* \ln(2)/\ln(0.85)$, and migrating cells can be followed over longer time periods.

The question then arises if cell migration through a 3D connective tissue matrix is influenced by the magnetic material. It seems plausible that intracellular super-clusters may increase the steric hindrance that cells experience when they migrate through narrow spaces and holes, or the clusters may disrupt the cytoskeletal architecture and hence the contractile machinery that drives cell motility in 3D. However, we find no such detrimental effects of the magnetic material. The contractile forces

applied by the cell on its surroundings (Fig. 6a,b) was not decreased, and the cells' ability to migrate through a 3D extracellular matrix (Fig. 6c) was not altered by the presence of intracellular iron oxide particles.

In a standard 1.5 T clinical MRI scanner, the detection limit of freshly labeled cells in agarose using the R2* relaxation rate was 25 cells/mm^3, corresponding to 19.6 μM of Fe_2O_3. Similar detection limits were obtained with a 4.7 T small animal MRI scanner (Bruker BioSpin 47/40). The detection limit above agarose from R2 measurements was 70 cells/mm^3 in a 1.5 T clinical scanner (Fig. 8a,b). Although the R2* sensitivity is higher compared to R2, the iron oxide specificity is noticeably lower. R2* maps show pronounced artifacts at material interfaces, and signal distortions at the highest nanoparticle concentrations. In addition, the R2* background of animal tissue can be higher than the R2 background, depending on water and fat content, echo time, and other scanning parameters, implying that R2 may possibly be more sensitive and specific than R2* for detecting iron oxide-loaded cancer cells in animals.

The total amount of intracellular iron remains constant over time periods of at least 3 weeks (Supporting Information Fig. 1A), but the magnetic properties of the nanoparticles are changed. The saturation magnetization of the particles inside the cell decreased from 66 to 0 emu/g after 13 days of incubation time (Fig. 7c). This indicates that the cells successively degrade the superparamagnetic iron oxide particles into free paramagnetic iron ions (14). This is also consistent to a previous study where over the course of 21 days, a continuous decrease in R2 was observed when dextran-coated iron oxide particles where incubated in various low-pH buffers (19). The relaxation rates (R1, R2, and R2*) also decreased with time but did not vanish to agarose background levels (Fig. 8c). In particular, R2 and R2* remain increased by approximately 50% above background, relative to the rates from freshly labeled cells.

CONCLUSION

This report shows that PLL-coated FSP γFe$_2$O$_3$ nanoparticles are easily internalized by cells and do not influence their invasion and migration behavior. They have excellent magnetic properties and thus can be used as an intracellular MRI contrast agent. However, the superparamagnetic nanoparticles are degraded by the intracellular environment to free paramagnetic iron ions within 14 days. Over this time period, the R1 contrast decreases dramatically, but the R2 and R2* contrast remains elevated at approximately 50% of the contrast seen in freshly labeled cells. Furthermore, the partitioning of the iron oxide particles during cell division among the daughter cells also leads to a decreasing MRI contrast over time. Both processes must be taken into account when γFe$_2$O$_3$ particles are used as an MRI contrast agent for long-term studies of cell migration in vivo.

REFERENCES

1. Bulte JWM, Zhang SC, van Gelderen P, Herynek V, Jordan EK, Duncan ID, Frank JA. Neurotransplantation of magnetically labeled oligodendrocyte progenitors: Magnetic resonance tracking of cell migration and myelination. Proc Nat Acad Sci USA 1999;96:15256–15261.
2. Foster PJ, Dunn EA, Karl KE, Snir JA, Nycz CM, Harvey AJ, Pettis RJ. Cellular magnetic resonance imaging: in vivo imaging of melanoma cells in lymph nodes of mice. Neoplasia 2008;10:207–216.
3. Arbab AS, Bashaw LA, Miller BR, Jordan EK, Lewis BK, Kalish H, Frank JA. Characterization of biophysical and metabolic properties of cells labeled with superparamagnetic iron oxide nanoparticles and transfection agent for cellular MR imaging. Radiology 2003;229:838–846.
4. Wang L, Liu HW, McNeill KD, Stelmack G, Scott JE, Halayko AJ. Mechanical strain inhibits airway smooth muscle gene transcription via protein kinase C signaling. Am J Respir Cell Mol Biol 2004;31:54–61.
5. Bos C, Delmas Y, Desmouliere A, et al. In vivo MR imaging of intravascularly injected magnetically labeled mesenchymal stem cells in rat kidney and liver. Radiology 2004;233:781–789.
6. Heymer A, Haddad D, Weber M, Gbureck U, Jakob PM, Eulert J, Noth U. Iron oxide labelling of human mesenchymal stem cells in collagen hydrogels for articular cartilage repair. Biomaterials 2008;29:1473–1483.
7. Bowen CV, Zhang X, Saab G, Gareau PJ, Rutt BK. Application of the static dephasing regime theory to superparamagnetic iron-oxide loaded cells. Magn Reson Med 2002;48:52–61.
8. Li D, Teoh WY, Selomulya C, Woodward RC, Munroe P, Amal R. Insight into microstructural and magnetic properties of flame-made gamma-Fe2O3 nanoparticles. J Mater Chem 2007;17:4876–4884.
9. Li D, Teoh WJ, Selomulya C, Woodward RC, Amal R, Rosche B. Flame-sprayed superparamagnetic bare and silica-coated maghemite nanoparticles: synthesis, characterization, and protein adsorption–desorption. Chem Mater 2006;18:6403–6413.
10. Kostura L, Kraitchman DL, Mackay AM, Pittenger MF, Bulte JW. Feridex labeling of mesenchymal stem cells inhibits chondrogenesis but not adipogenesis or osteogenesis. NMR Biomed 2004;17:513–517.
11. LeBel CP, Ischiropoulos H, Bondy SC. Evaluation of the probe 2′,7′-dichlorofluorescin as an indicator of reactive oxygen species formation and oxidative stress. Chem Res Toxicol 1992;5:227–231.
12. Koch TM, Muenster S, Bonakdar N, Buttler JP, Fabry B. 3D traction forces in cancer cell invasion. PLoS One 2012;7:e33476.
13. Mierke CT, Frey B, Fellner M, Herrmann M, Fabry B. Integrin {alpha}5{beta}1 facilitates cancer cell invasion through enhanced contractile forces. J Cell Sci 2010;124(Pt 3):369–383.
14. Levy M, Lagarde F, Maraloiu VA, Blanchin MG, Gendron F, Wilhelm C, Gazeau F. Degradability of superparamagnetic nanoparticles in a model of intracellular environment: follow-up of magnetic, structural and chemical properties. Nanotechnology 2010;21:395103.
15. Riemer J, Hoepken HH, Czerwinska H, Robinson SR, Dringen R. Colorimetric ferrozine-based assay for the quantitation of iron in cultured cells. Anal Biochem 2004;331:370–375.
16. Vuong QL, Gillis P, Gossuin Y. Monte Carlo simulation and theory of proton NMR transverse relaxation induced by aggregation of magnetic particles used as MRI contrast agents. J Magn Reson 2011;212:139–148.
17. Carroll MRJ, Woodward RC, House MJ, Teoh WY, Amal R, Hanley TL, St Pierre TG. Experimental validation of proton transverse relaxivity models for superparamagnetic nanoparticle MRI contrast agents. Nanotechnology 2010;21:035103.
18. Huang G, Chen H, Dong Y, Luo X, Yu H, Moore Z, Bey EA, Boothman DA, Gao J. Superparamagnetic iron oxide nanoparticles: amplifying ROS stress to improve anticancer drug efficacy. Theranostics 2013;3:116–126.
19. Arbab AS, Wilson LB, Ashari P, Jordan EK, Lewis BK, Frank JA. A model of lysosomal metabolism of dextran coated superparamagnetic iron oxide (SPIO) nanoparticles: implications for cellular magnetic resonance imaging. NMR Biomed 2005;18:383–389.